Ships and Offshore Structures

ISSN: (Print) (Online) Journal homepage: https://www.tandfonline.com/loi/tsos20

Numerical investigation of breaking wave loads on the downstream inclined cylinder under shelter effect from the upstream vertical cylinder

Sen Qu, Huilong Ren, Shengnan Liu, Shuzheng Sun & Muk Chen Ong

To cite this article: Sen Qu, Huilong Ren, Shengnan Liu, Shuzheng Sun & Muk Chen Ong (2021): Numerical investigation of breaking wave loads on the downstream inclined cylinder under shelter effect from the upstream vertical cylinder, Ships and Offshore Structures, DOI: 10.1080/17445302.2021.1937854

To link to this article: https://doi.org/10.1080/17445302.2021.1937854

Published online: 15 Jun 2021.

SHIPS AND OFFSHORE STRUCTURES
https://doi.org/10.1080/17445302.2021.1937854

Taylor & Francis
Taylor & Francis Group

Numerical investigation of breaking wave loads on the downstream inclined cylinder under shelter effect from the upstream vertical cylinder

Sen Qu[a], Huilong Ren[a], Shengnan Liu [b], Shuzheng Sun[a] and Muk Chen Ong[b]

[a]College of Shipbuilding Engineering, Harbin Engineering University, Harbin, People's Republic of China; [b]Department of Mechanical and Structural Engineering and Materials Science, University of Stavanger, Stavanger, Norway

ABSTRACT

Breaking waves interaction with two tandem cylinders are numerically studied using Computational Fluid Dynamic (CFD) software OpenFOAM. The effects of transverse inclined angles of the downstream cylinder and separation distances between two cylinders on breaking wave loads and free surface elevations are investigated. The interface between air and water phases is captured by the Volume of Fluid (VOF) method. The Shear Stress Transport $k-\omega$ ($SST\ k-\omega$) turbulence model is employed to solve the incompressible Reynolds-Averaged Navier-Stokes (RANS) equations. The present numerical model is validated against published experimental data by examining the horizontal breaking wave loads and free surface elevations of breaking waves past a vertical cylinder and an inclined cylinder. In the present incident wave conditions, the breaking wave force on the downstream cylinder decreases first and then increases with the transverse inclined angle varying from 0° to 30°, while it shows an opposite trend versus the distance between cylinders. The maximum breaking wave load on the downstream cylinder occurs when the it is installed vertically with a separation distance of four times diameter.

ARTICLE HISTORY
Received 30 November 2020
Accepted 26 May 2021

KEYWORDS
Breaking wave; tandem cylinders; transverse inclined angles; $SST\ k-\omega$ turbulence model; CFD

1. Introduction

Multiple circular cylinders can be commonly seen in wind turbines, offshore platforms and large pontoons as supporting structural components. In shallow water, marine structures are usually subject to highly nonlinear breaking wave loads. When breaking wave past cylinders group, the upstream cylinder will affect the hydrodynamic forces on the downstream cylinder. Understanding the interaction characteristics of breaking wave interacting with multiple cylinders are of great importance for engineering design to ensure structural safety in extreme conditions.

Experiment is an essential investigation for the breaking wave-structure interaction problem directly. Sawaragi and Nochino (1984) performed an experiment of breaking waves past a vertical cylinder. The experimental results showed that the position of wave breaking had significant effect for wave impacting forces. They found that the rising time of the wave impacting force was related to the front shape of the breaking wave while hitting the cylinder. Apelt and Piorewicz (1986) studied the breaking wave loads on vertical cylinders perpendicular and parallel to the wave propagation direction. They found that the steepness of the incident wave and the distance between cylinders had significant effects on the breaking wave force, and the effect was more obvious for the cylinders perpendicular to the wave direction than the cylinders parallel to the wave direction. Wienke et al. (2001) studied breaking wave loads on a vertical cylinder experimentally. It was found that the breaking wave force calculated by Morison formula was smaller than the experimental measurement, and the impact force considering the magnitude and duration of the impact was suggested to add into the Morison equation. Irschik et al. (2004) performed large-scale experiments of breaking waves past a vertical cylinder and inclined cylinders. The inclined angles of cylinders were parallel to the wave propagation direction. They employed Fast Fourier Transform (FFT) low-pass filter with the Empirical Mode Decomposition (EMD) method to divide the experimental breaking wave forces into the quasi-static load and the dynamic load. The experimental results showed that the cylinder was subjected to the largest wave impact when the wave broke exactly in front of the cylinder. Sparboom et al. (2005) investigated the breaking wave loads on multi-vertical cylinders by a series of experimental tests. The breaking wave load on the lee-side cylinder decreased significantly due to the strong shelter effect from the upstream cylinder. Esandi et al. (2020) performed an experimental study for the spilling breaking waves and non-breaking waves past a vertical cylinder. The experimental results showed that the spilling breaking wave produced a larger force on the cylinder as compared to the non-breaking wave. Ha et al. (2020) analyzed the effects of air bubbles on the breaking wave forces on the vertical cylinder by carrying out experimental tests in the wave tank. They found that the wave loads increased as the wave breaking point approaching the cylinder. Ma et al. (2020) performed an experiment of plunging solitary waves past a vertical cylinder. The experimental results showed that the maximum measured forces occurred when the front of wave crest just curled down prior to touch the water surface.

In addition to experimental investigation, Computational Fluid Dynamics (CFD) can provide the accurate calculation for physical features of breaking waves interaction with cylinders in more details. Christensen et al. (2005) numerically simulated the breaking waves past a vertical cylinder with the volume of fluid (VOF) method. They pointed out that the breaking wave load increased significantly from spilling breaker to plunging breaker. Xiao and

CONTACT Shengnan Liu liushengnan003@gmail.com Department of Mechanical and Structural Engineering and Materials Science, University of Stavanger, Stavanger 4036, Norway

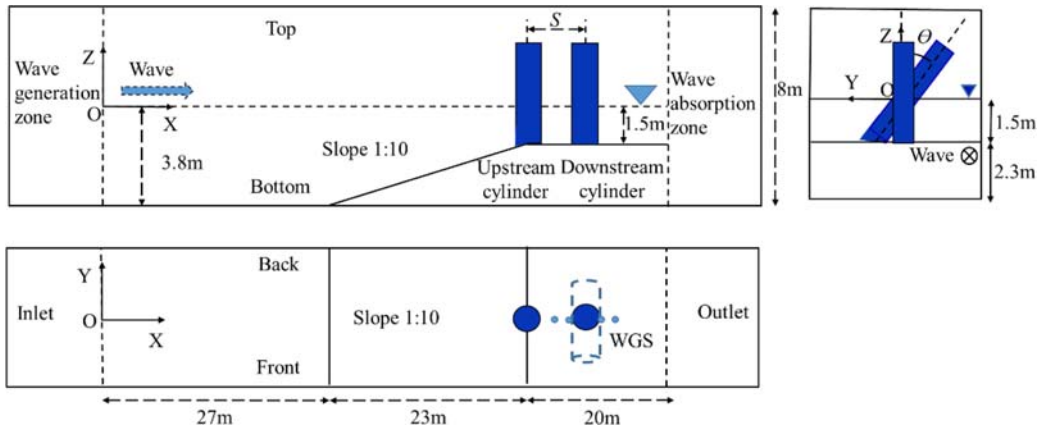

Figure 1. Numerical setup for three-dimensional numerical wave tank. (This figure is available in colour online.)

Table 1. Overview of simulation cases under different initial parameters for breaking wave past two tandem cylinders.

Scenario	θ(°)	S(m)	F(kN)
A	0	3D	11.93
		4D	12.66
		5D	9.63
B	15	3D	8.46
		4D	10.23
		5D	7.51
C	30	3D	10.46
		4D	12.24
		5D	8.07

Huang (2015) used the $k-\varepsilon$ turbulence model to predict breaking waves force on vertical cylinders, which were placed at different elevations from the plane beach. When the cylinder was placed at 3/4 H (H is the maximum vertical run-up height) below the shoreline, the largest breaking wave force can be obtained. Choi et al. (2015) applied modified Navier-Stokes (NS) equations in combination with the VOF method to predict breaking wave loads on a vertical cylinder and an inclined cylinder, which was parallel to the wave propagation direction. The effect of cylinder's vibration in the experiment on the impacting force was investigated. The numerically predicted breaking wave forces agreed well with the original experimental measurement data processed by FFT low pass filter and EMD. They also compared the original experimental data with calculated breaking wave forces processed by Duhamel integral to validate the method proposed above. Kamath et al. (2016) employed the $k-\omega$ turbulence model with the level set method (LSM) to analyze the effects of wave breaking points on impacting force acting on a vertical cylinder. Their numerical results showed that the maximum breaking wave force was observed when the front of wave tongue just overturned and acted on the surface of the vertical cylinder. Based on the research of Kamath et al. (2016), Bihs et al. (2016) simulated the breaking waves passing through two vertical cylinders arranging in tandem. The sheltering effect from the upstream cylinder reduced the wave load on the downstream cylinder in the case of the wave breaking before it touching the upstream cylinder. The variations of water jet and reconnection of separated wave crest behind the upstream cylinder also produced a significant impact on the force on the downstream cylinder. Chow et al. (2019) used an improved incompressible smoothed particle hydrodynamic (ISPH) method to simulate the process of non-breaking waves and breaking waves past a vertical cylinder. They found that the steepness of the wave and the free surface elevation were two critical factors to affect the maximum

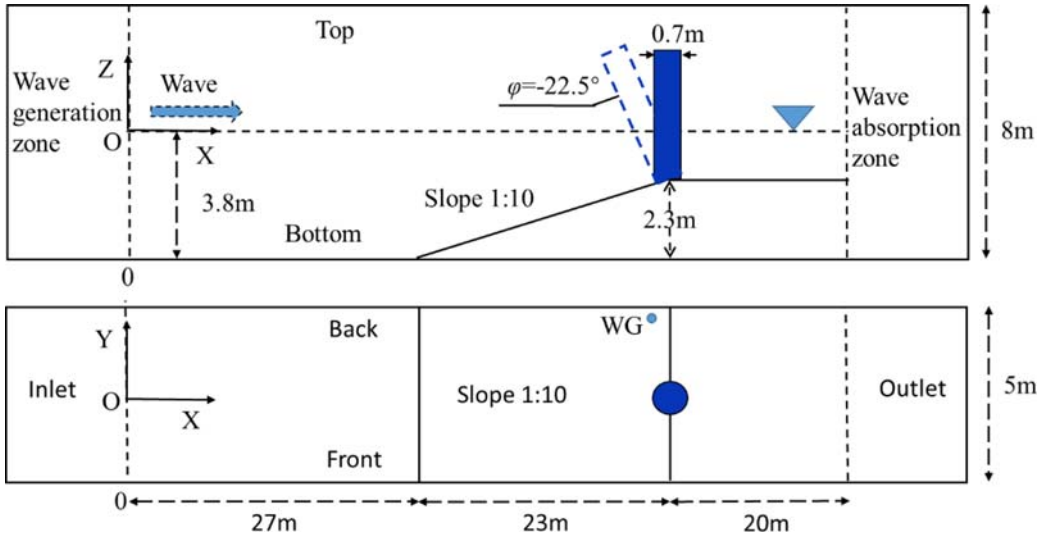

Figure 2. Side view (top) and top view (bottom) of the numerical wave tank (NWT) for validation study. (This figure is available in colour online.)

impacting force on the structure. As compared with the non-breaking waves, the cylinder under the action of breaking waves suffered higher local pressures near the free surface.

Recently, Liu et al. (2019a) numerically investigated the characteristics of the breaking wave forces on the vertical cylinder using the Shear Stress Transport $k-\omega$ ($SST\,k-\omega$) turbulence model with the VOF method. The calculated results showed that the higher-harmonic wave force can be produced by the slamming wave force and the secondary load under condition of the breaking wave impacting on the vertical cylinder. Then, Liu et al. (2019b) simulated the process of breaking waves passing through a vertical cylinder with different Keulegan–Carpenter (KC) numbers using the same numerical model. Their results showed that the peak value of the breaking wave load on the structure and the horizontal velocity of the water particle at wave front increase with the increasing KC number. Qu et al. (2020) employed the $SST\,k-\omega$ turbulence model with the VOF method to simulate the interaction between the breaking wave and transverse inclined cylinders, which were perpendicular to the wave propagation direction. The FFT filter was used to separate the low-order and high-order wave forces from the total breaking wave force acting on the cylinder. The minimum value of the normalized high-order wave force could be observed and the phenomenon of secondary load was disappeared under the circumstance of the cylinder placed with a transverse inclined angle 45°. Tang et al. (2020) numerically investigated the characteristics of different breaking waves' interactions with the vertical offshore wind turbines by solving the Navier-Stokes equations. The curve of the surface elevation presented multi-peaks under a plunging wave type and was more irregular as compared a spilling wave type.

In general, most literature studied the effects of the incident wave steepness, wave breaking points, cylinder's vibration, and numerical methods on the wave impact force on the single cylinder. A few articles also investigated breaking wave loads on multiple vertical cylinders by examining different distances between cylinders and the arrangement of cylinders. However, limited research focuses on simulating the breaking wave past a pair of tandem cylinders with different transverse inclined angles, which commonly appear in marine structures. The main purpose of the present paper is to study the effects of transverse inclined angles and distances between two cylinders on breaking wave loads, especially for the downstream cylinder under the shelter effect from the upstream vertical cylinder. The present research employs the $SST\,k-\omega$ turbulent model (Menter et al. 2003) to capture the turbulence characteristics, which effectively blends the $k-\varepsilon$ turbulence model in the far-field and $k-\omega$ turbulence model in the near-wall region. It avoids the problem that the $k-\omega$ turbulence model is very sensitive to the inlet free-stream turbulence properties. The $SST\,k-\omega$ turbulent model can provide proper behavior in prediction of the free surface elevation and the breaking wave force, which has been used in the previous studies (Liu et al. 2019a; Liu et al. 2019b; Qu et al. 2020) for simulating the breaking wave past a vertical cylinder. The numerical simulations are carried out by an open-source CFD software OpenFOAM.

The rest of this paper is structured as follows. Section 2 presents the governing equations and the turbulence model. Then, the setup of numerical wave tank is presented in Section 3. Section 4 shows the validation study of the present model by comparing the numerical results and published experimental data for two cases of the breaking waves interaction with a vertical cylinder and an inclined cylinder. Meanwhile, the features of breaking wave loads on the downstream cylinder and the variations of free surface elevations around the downstream cylinders under different scenarios are analyzed. Finally, the main conclusions are drawn in Section 5.

2. Numerical implementation

2.1. Numerical model

The numerical model is based on the incompressible Reynolds-Averaged Navier-Stokes (RANS) equations.

$$\frac{\partial u_i}{\partial t}+u_j\frac{\partial u_i}{\partial x_j}=-\frac{1}{\rho}\frac{\partial p_{rgh}}{\partial x_i}+\nu\frac{\partial^2 u_i}{\partial x_j^2}-\frac{\partial\overline{u_i'u_j'}}{\partial x_j} \tag{1}$$

$$\frac{\partial u_i}{\partial x_i}=0 \tag{2}$$

where u_i are the fluid velocity in Cartesian components, p_{rgh} denotes the pressure in excess of the hydrostatic pressure, ρ means the fluid density, and ν presents the kinematic viscosity. $\overline{u_i'u_j'}$ is the Reynolds stress component, which is expressed using the Boussinesq approximation.

$$\overline{u_i'u_j'}=\nu_t\left(\frac{\partial u_i}{\partial x_j}+\frac{\partial u_j}{\partial x_i}\right)-\frac{2}{3}k\delta_{ij} \tag{3}$$

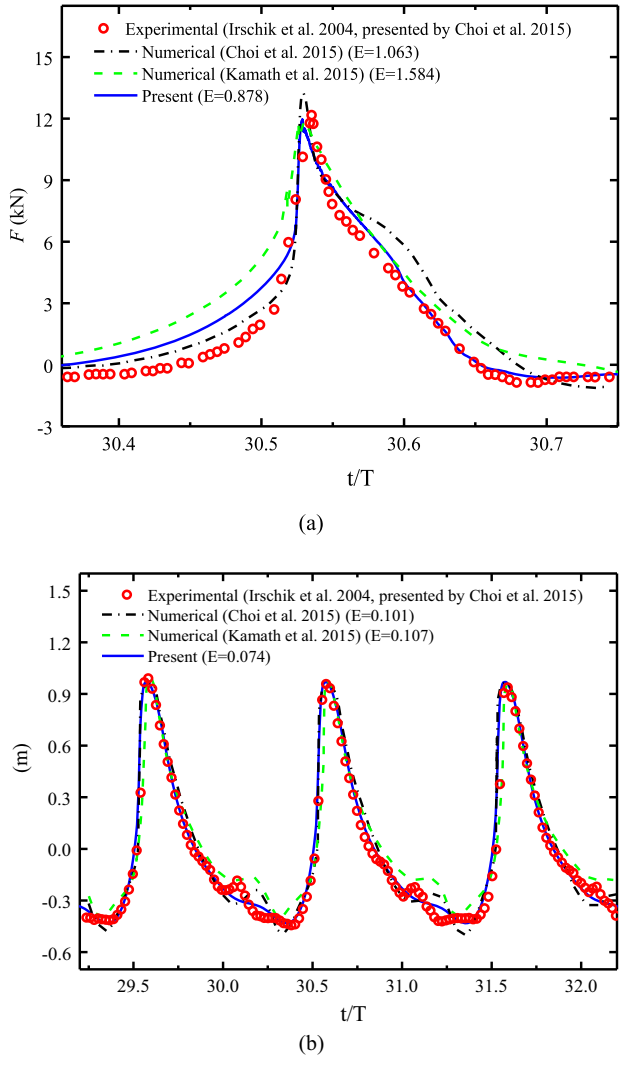

Figure 3. Comparisons of the present numerical results with the published data for breaking wave past a vertical cylinder: (a) breaking wave forces over one wave period; (b) free surface elevations at WG location over three wave periods. RMSE values E, are calculated for breaking wave forces and free surface elevations with respect to the experimental data. (This figure is available in colour online.)

Here, the ν_t, k and δ_{ij} denotes the turbulent kinematic viscosity, turbulent kinetic energy and Kronecker delta, respectively.

The $SSTk-\omega$ turbulent model (Menter et al. 2003) is used to simulate the breaking wave past two cylinders. The two equations of turbulent kinetic energy k and specific rate of dissipation ω are expressed as:

$$\frac{\partial(\rho k)}{\partial t}+\frac{\partial(\rho u_i k)}{\partial x_i}=\frac{\partial}{\partial x_i}\left[(\mu+\sigma_k\mu_t)\frac{\partial k}{\partial x_i}\right]+P_k-\beta^*\rho\omega k \quad (4)$$

$$\frac{\partial(\rho\omega)}{\partial t}+\frac{\partial(\rho u_i\omega)}{\partial x_i}=\frac{\partial}{\partial x_i}\left[(\mu+\sigma_\omega\mu_t)\frac{\partial\omega}{\partial x_i}\right]+\alpha\rho Q^2-\beta\rho\omega^2+2(1-F_1)\frac{\rho\sigma_{\omega2}}{\omega}\frac{\partial k}{\partial x_i}\frac{\partial\omega}{\partial x_i} \quad (5)$$

where F_1 is the first blending function:

$$F_1=\tanh\left\{\left\{\min\left[\max\left(\frac{\sqrt{k}}{\beta^*\omega y},\frac{500\nu}{y^2\omega}\right),\frac{4\rho\sigma_{\omega2}k}{CD_{k\omega}y^2}\right]\right\}^4\right\} \quad (6)$$

$$CD_{k\omega}=\max\left(2\frac{\rho\sigma_{\omega2}}{\omega}\frac{\partial k}{\partial x_i}\frac{\partial\omega}{\partial x_i},10^{-10}\right) \quad (7)$$

where y is the distance between the wall and the center of the first layer grid. The dynamic turbulent viscosity μ_t is given by:

$$\mu_t=\frac{\rho a_1 k}{\max(a_1\omega, QF_2)} \quad (8)$$

where $Q=\sqrt{2Q_{ij}Q_{ij}}$ is the invariant measure of the strain rate. $Q_{ij}=\frac{1}{2}\left(\frac{\partial u_i}{\partial x_j}+\frac{\partial u_j}{\partial x_i}\right)$ is the mean rotation rate tensor. F_2 is the

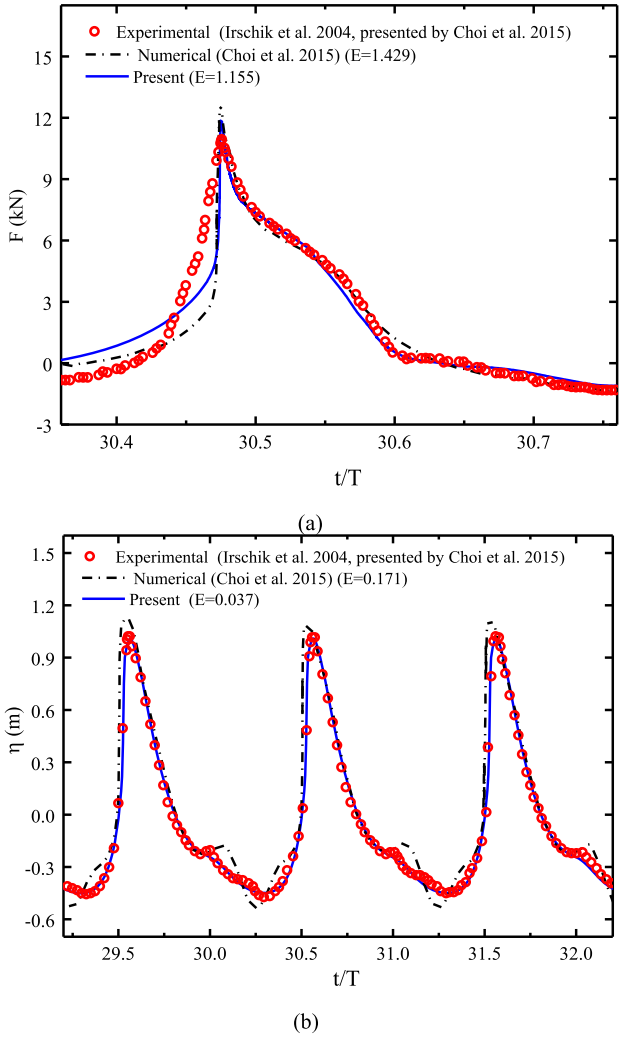

Figure 4. Comparisons of the present numerical results with the published data for breaking wave past an inclined cylinder ($\varphi=-22.5°$): (a) breaking wave forces over one wave period; (b) free surface elevations at WG location over three wave periods. RMSE values E, are calculated for breaking wave forces and free surface elevations with respect to the experimental data. (This figure is available in colour online.)

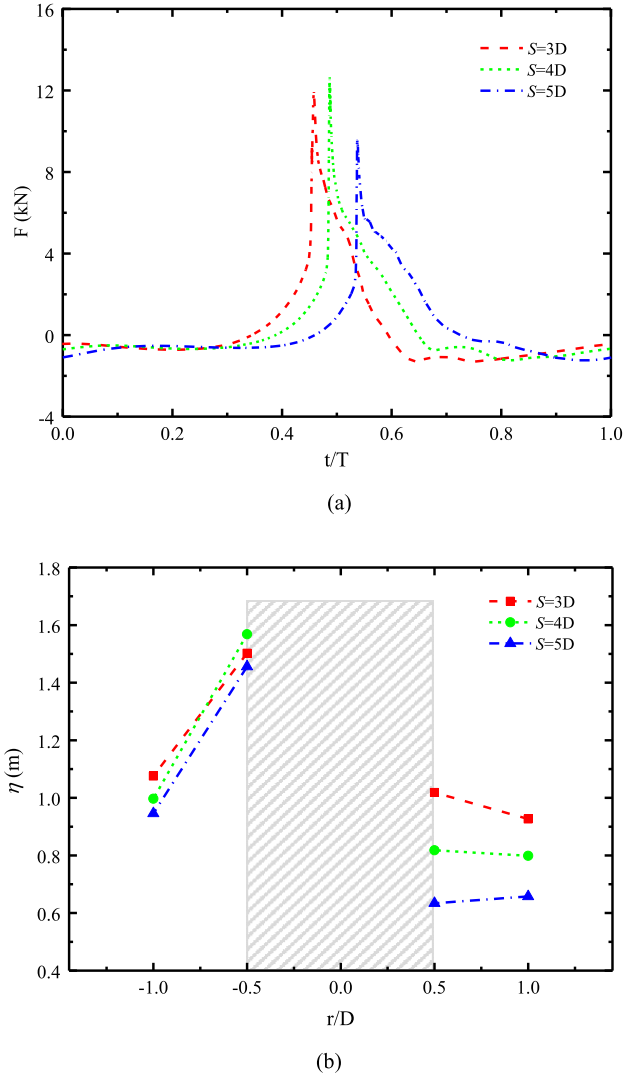

Figure 5. Variations of breaking wave forces and peaks of free surface elevations under different distance S for Scenario A ($\theta=0°$): (a) breaking wave forces on the downstream cylinder; (b) peaks of free surface elevations around the downstream cylinder. (This figure is available in colour online.)

second blending function expressed by

$$F_2 = \tanh\left[\left[\max\left(\frac{2\sqrt{k}}{\beta^* \omega y}, \frac{500\nu}{y^2 \omega}\right)\right]^2\right] \tag{9}$$

The production term $P_k = \min(G, 10\beta^* \rho k \omega)$, where G is given by

$$G = \mu_t \frac{\partial u_i}{\partial x_j}\left(\frac{\partial u_i}{\partial x_j} + \frac{\partial u_j}{\partial x_i}\right) \tag{10}$$

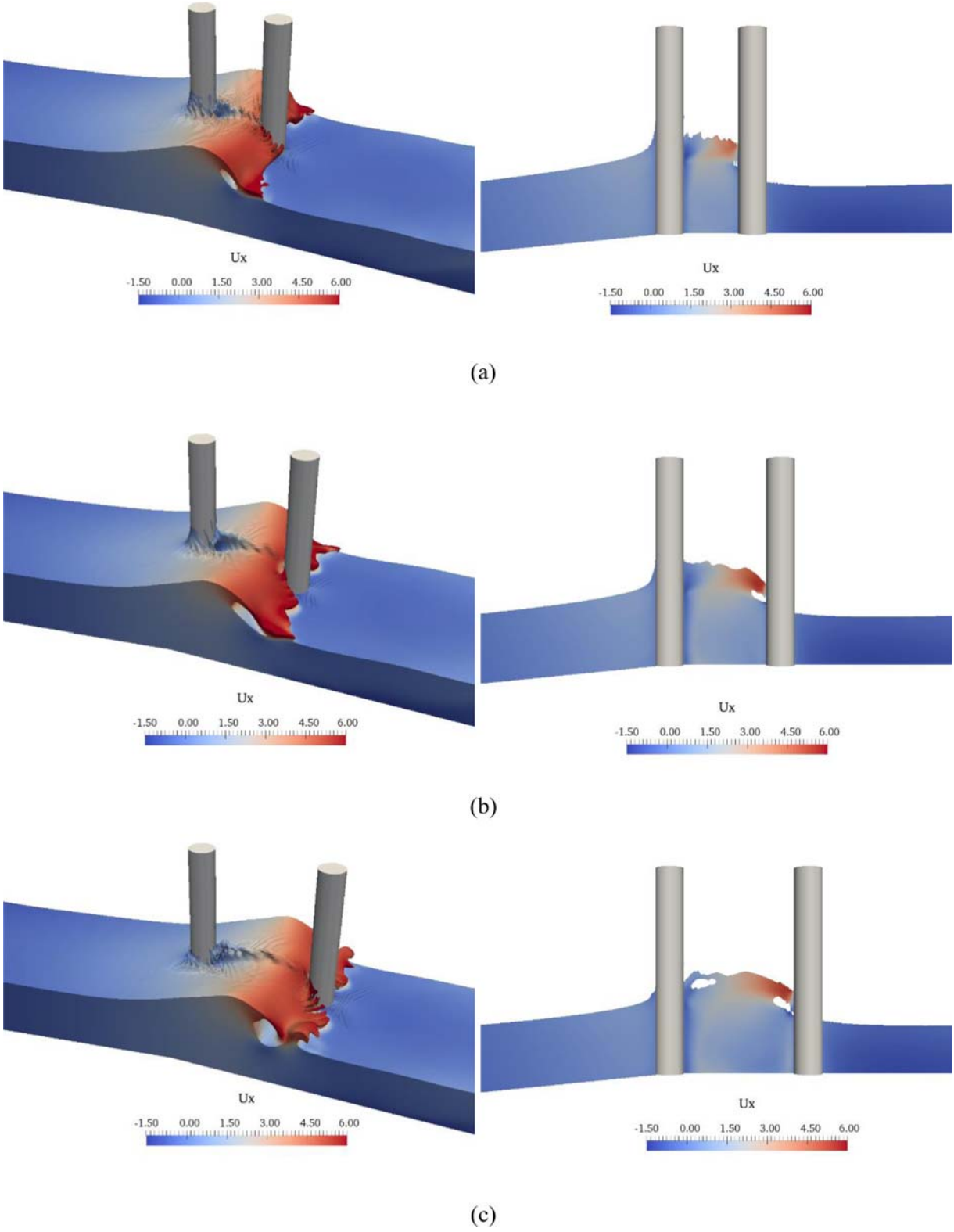

Figure 6. Snapshots of wave surface with horizontal velocity contours corresponding to the time of maximum wave load on the downstream cylinder for Scenario A: (a) $S = 3D$; (b) $S = 4D$; (c) $S = 5D$. The left side is a three-dimensional view, and the right side is a section view passing through the central axis of the downstream cylinder and the origin of the coordinates. (This figure is available in colour online.)

The values of α_k, α_ω, α and β are blended using the equation:

$$\phi = F_1\phi_1 + (1 - F_1)\phi_2 \tag{11}$$

The constants for this model are: $\alpha_1 = 5/9$, $\alpha_2 = 0.44$, $\beta_1 = 0.075$, $\beta_2 = 0.0828$, $\sigma_{k1} = 0.85$, $\sigma_{k2} = 1$, $\sigma_{\omega1} = 0.5$, $\sigma_{\omega2} = 0.856$, $\beta^* = 0.09$.

2.2. Free surface capture

The VOF method (Hirt and Nichols 1981) is based on a volume fraction coefficient α, which is 0 for air, 1 for water, and in between 0 and 1 for mixture interface of the two fluids. The volume fraction can be obtained by solving the follow advection equation:

$$\frac{\partial\alpha}{\partial t} + \frac{\partial(\alpha u_i)}{\partial x_i} + \frac{\partial[\alpha(1-\alpha)u_{ir}]}{\partial x_i} = 0 \tag{12}$$

where u_{ir} is the relative velocity of the water and the air in the direction normal to the interface. The densities and kinematic viscosities of water (ρ_w, ν_w), and air (ρ_a, ν_a), at the interface are given by

$$\begin{cases} \rho = \alpha\rho_w + (1-\alpha)\rho_a \\ \nu = \alpha\nu_w + (1-\alpha)\nu_a \end{cases} \tag{13}$$

2.3. Numerical wave tank

The wave is generated and absorbed by waves2Foam, a package of the open-source CFD software OpenFOAM. The relaxation algorithm proposed by Jacobsen et al. (2012) is used to avoid wave reflection at the inlet boundary and outlet boundary of the numerical wave tank (NWT). The velocity $u_i$and the volume fraction α inside relaxation zones are expressed by

$$\begin{aligned} u_i &= \gamma_R u_{icomputed} + (1-\gamma_R)u_{itarget} \\ \alpha &= \gamma_R \alpha_{\text{computed}} + (1-\gamma_R)\alpha_{\text{target}} \end{aligned} \tag{14}$$

where the weighting factor γ_R is defined as:

$$\gamma_R = 1 - \frac{\exp(\chi_R^{3.5}) - 1}{\exp(1) - 1}, \chi_R \in [0, 1] \tag{15}$$

In this paper, the PIMPLE algorithm is used to solve the coupling problem of pressure and velocity. The second-order implicit Crank–Nicolson scheme is applied for the discretization of time domain. The second-order Gauss integration with linear interpolation combining a limited coefficient is used for the convective terms. The second-order Gauss integration with linear interpolation is employed for the diffusive terms.

3. Setup for numerical simulations

Figure 1 shows the sketch of numerical wave tank (NWT). The NWT is 120 m long and 8 m high. The width of NWT is changed with the transverse inclined angle of the downstream cylinder, leaving at least 4D distance (D = 0.7 m is diameter of cylinder) between two ends of the cylinder and front-back boundaries of NWT to avoid the effects of the sidewalls on the simulated results. The still water depth is 3.8 m. The transverse inclined angle θ is defined as the angle between the central axis of downstream cylinder and the Z axis in the YZ plane. The rotation center of the downstream cylinder is at the still water plane (Z = 0). The upstream cylinder is vertically fixed at the end of the slope (1:10). The center-to-center distance between two cylinders is defined as *S*. Wave gauges (WGS) are placed at the plane (Y = 0) passing through the rotation center of the downstream cylinder with horizontal locations r/D = -1, -0.5, 0.5, 1 (r is the distance to the central axis of the downstream cylinder). The different combinations of three distances (*S* = 3D, 4D, 5D) and three transverse inclined angles (θ = 0°, 15°, 30°) of the downstream cylinder, total nine cases are simulated as shown in Table 1, where *F* is horizontal breaking wave load on the downstream cylinder. In the present paper, incident wave parameters with wave period *T* = 4.0 s and wave height *H* = 1.3 m are fixed for all simulation cases, which ensures the wave breaking in front of the upstream cylinder (Liu et al. 2019a; Liu et al. 2019b; Qu et al. 2020).

At the inlet domain of NWT, the water velocity is obtained from the wave theory and the air velocity is set to zero, the pressure is specified as zero gradient condition. The velocities of water and air for outlet boundary are set to zero and the pressure is specified as zero gradient condition. On the top domain, the *pressureInletOutletVelocity* condition is applied to the velocity, which means that the inflow velocity is computed from the flux in the patch-normal direction and the outflow velocity is set as zero gradient boundary. The *totalPressure* is employed for pressure, which is equal to the difference between the total pressure and the dynamic pressure.

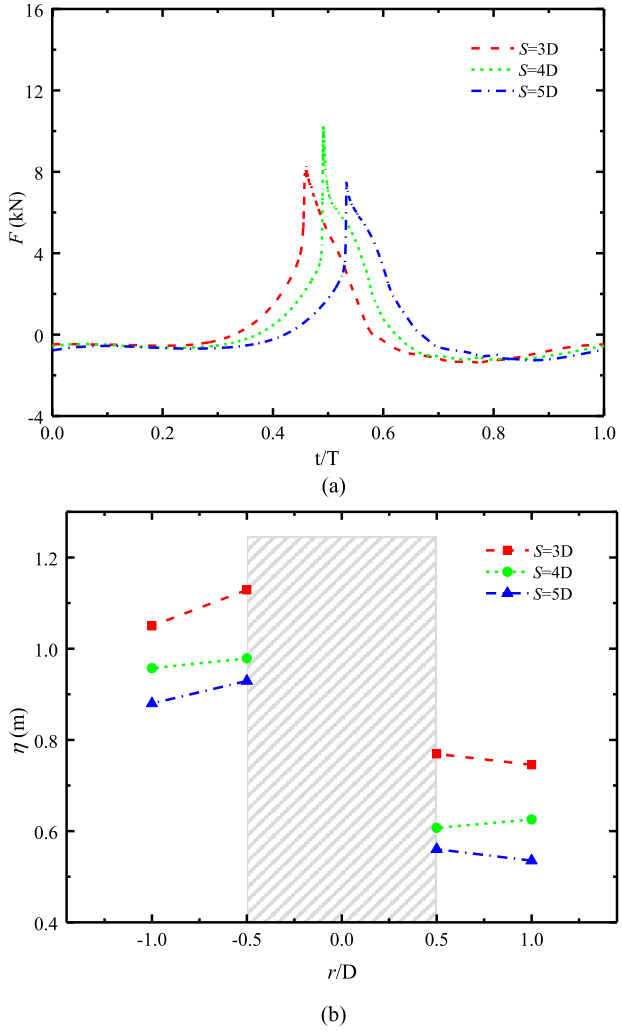

Figure 7. Variations of breaking wave forces and peaks of free surface elevations under different distance *S* for Scenario B (θ = 15°): (a) breaking wave forces on the downstream cylinder; (b) peaks of free surface elevations around the downstream cylinder. (This figure is available in colour online.)

The zero normal gradient condition for pressure and the no-slip condition for velocity are employed on the bottom of NWT and cylinder's surface. Meanwhile, the wall functions are used to simulate characteristics of the boundary layer. The dimensionless wall distance y^+varies between 40 and 200 within one wave period for the present simulation.

The grid size around the cylinder and the free surface is refined. Grid and time-step convergence studies on the breaking wave load

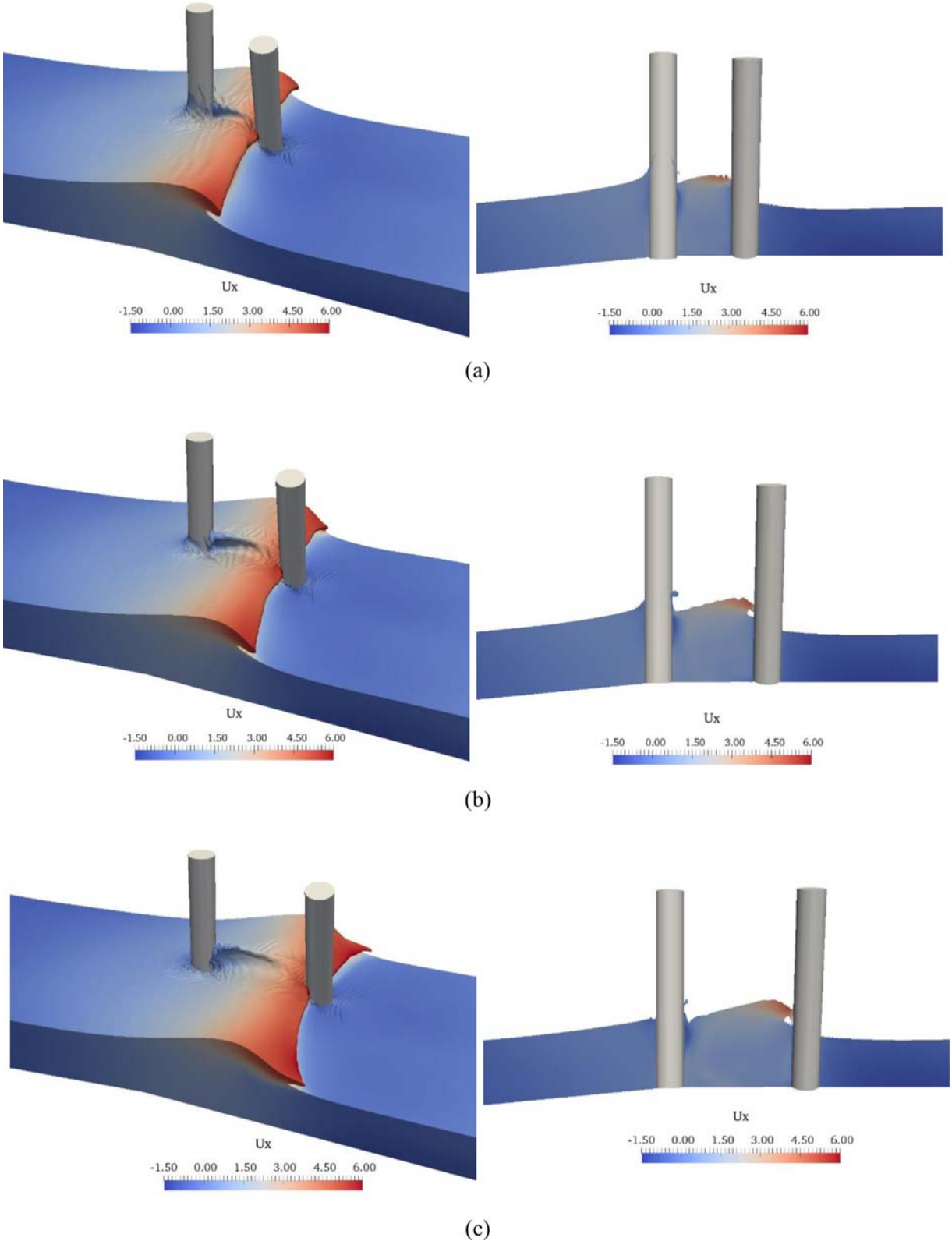

Figure 8. Snapshots of free surface with horizontal velocity contours corresponding to the time of maximum breaking wave force on the downstream cylinder for Scenario B: (a) $S = 3D$; (b) $S = 4D$; (c) $S = 5D$. The left side is a three-dimensional view, and the right side is a section view passing through the central axis of the downstream cylinder and the origin of the coordinates. (This figure is available in colour online.)

and the free surface elevation around single vertical cylinder have been carried out in previous paper (Qu et al. 2020). Eventually, the medium mesh of maximum $dx = 0.1$m and the maximum Courant number 0.5 are used to simulate the numerical results with sufficient accuracy.

4. Results

4.1. Validation of the numerical model

Irschik et al. (2004) performed an experiment for breaking waves load on a cylinder placed with different inclined angles at the Large Wave Channel (GWK) in Hannover, Germany. The diameter of cylinder is D = 0.7m, and its central axis was located at the end of the slop (1:10). Two cases of the cylinder with a vertical angle and an inclined angle $\varphi = -22.5^{o}$ are selected to validate the accuracy of numerical model by comparing the breaking wave force and the free surface elevation between the experimental data and the numerical results. The φ is parallel and positive to the direction of wave propagation. Based on the experimental setup, the validated NWT is 120.0 m long, 8 m high and 5 m wide with a still water depth 3.8 m. A cylinder ($D = 0.7m$) is installed at $x = 50$m with different angles. The details can be seen in Figure 2. The wave gauge (WG) is located near the sidewall along the frontline of the cylinder to measure variations of free surface elevations.

Figure 3 shows the comparisons of the horizontal breaking wave forces F on the vertical cylinder and the free surface elevations η at WG position between the present numerical results and the published data (Irschik et al. 2004). The E denotes root mean square error (RMSE), which is calculated with respect to the experimental data (indicated by red dots in Figure 3) for the breaking wave forces and the surface elevations. The RMSE of the present numerical breaking wave force is smaller than that from Choi et al. (2015) and Kamath et al. (2016) shown in Figure 3(a). Meanwhile, the relative error of the maximum breaking wave force between the present result and the experimental data (Choi et al. (2015) removed the effect of cylinder vibration from the initial experimental results (Irschik et al. 2004)) is 0.7%, which is lower than relative errors 1.2% and 10.1% from Choi et al. (2015) and Kamath et al. (2016) respectively. It shows that the present predicted breaking wave forces agree well with the experimental data. For the prediction of free surface elevations at WG in Figure 3(b), the present simulated result is better than other numerical simulation results comparing with the experimental data, which is indicated by the smaller RMSE values for surface elevations calculated using the present model.

The second validation case is performed by simulating the interaction between breaking waves and a cylinder with inclined angle $\varphi = -22.5^{o}$. The present calculated the breaking wave loads and the free surface elevations are compared with the published data presented by Choi et al. (2015) in Figure 4(a) and Figure 4(b), respectively. The relative error of the breaking wave force between the present result and experimental data is 8.3%, which is smaller than 16.3% calculated by Choi et al. (2015). In terms of the free surface elevations, the present results agree well with the experimental data with a lower RMSE value as compared to results from Choi et al. (2015) and Kamath et al. (2016). Two validation cases suggest that the present numerical model has sufficient accuracy for the interaction between the breaking wave and the cylinder.

4.2. Variations of breaking wave forces and free surface elevations with different scenarios

Figure 5(a) shows variations of breaking wave impacting forces F on the downstream cylinder versus different separation distance S over one wave period for Scenario A. It clearly shows that the wave impacting force calculated in the case of $S = 4$D is slightly higher than that with other S. The minimum value of breaking wave load is obtained when the downstream cylinder is installed at $S = 5$D. The relative difference in peak value of the F between $S = 4$D and $S = 5$D is 23.9%. Figure 5(b) presents peaks of free surface elevations η around the downstream cylinder under different separation distance S. The free surface elevations at $r/D = -1$ gradually decreases with S varying from 3D to 5D. The waves run up on the front surface of the downstream cylinder ($r/D = -0.5$). The largest free surface elevation is observed for the case of $S = 4$D where the relative difference is increased 57.3% from $r/D = -1$ to $r/D = -0.5$. For variation of surface elevations behind the downstream cylinder, the peaks value at both $r/D = 0.5$ and $r/D = 1$ decrease as S increases.

Further insight into the mechanism of interaction between the breaking wave and two tandem cylinders for Scenario A, the air–water interface around two cylinders with horizontal velocity Ux contours corresponding to the time of maximum wave loads on the downstream cylinder is presented in Figure 6. The wave crest separates first and then reconnects, and a water jet is formed

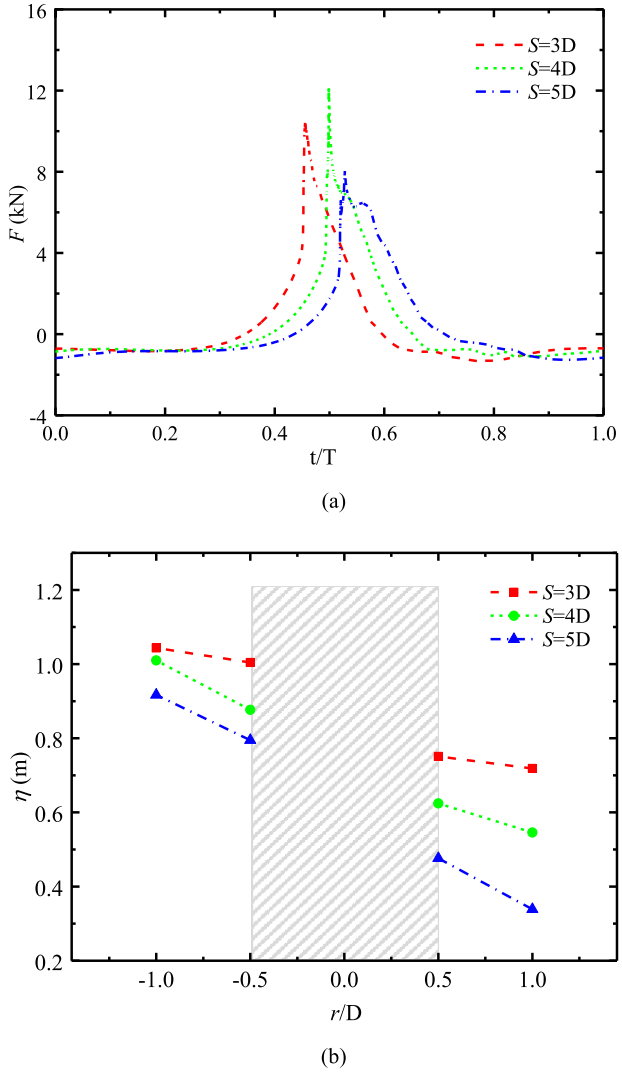

Figure 9. Variations of breaking wave forces and peaks of free surface elevations under different distance S for Scenario C ($\theta = 30^{o}$): (a) breaking wave forces on the downstream cylinder; (b) peaks of free surface elevations around the downstream cylinder. (This figure is available in colour online.)

when the breaking waves passing through the upstream cylinder installed vertically (Kamath et al. 2016). In Figure 6(a), for the case of $S = 3D$, the front of wave crest impacts horizontally on the downstream cylinder surface with a low horizontal velocity due to the close separation distance ($S = 3D$). While an overturned wave tongue acts on the downstream cylinder when the distance

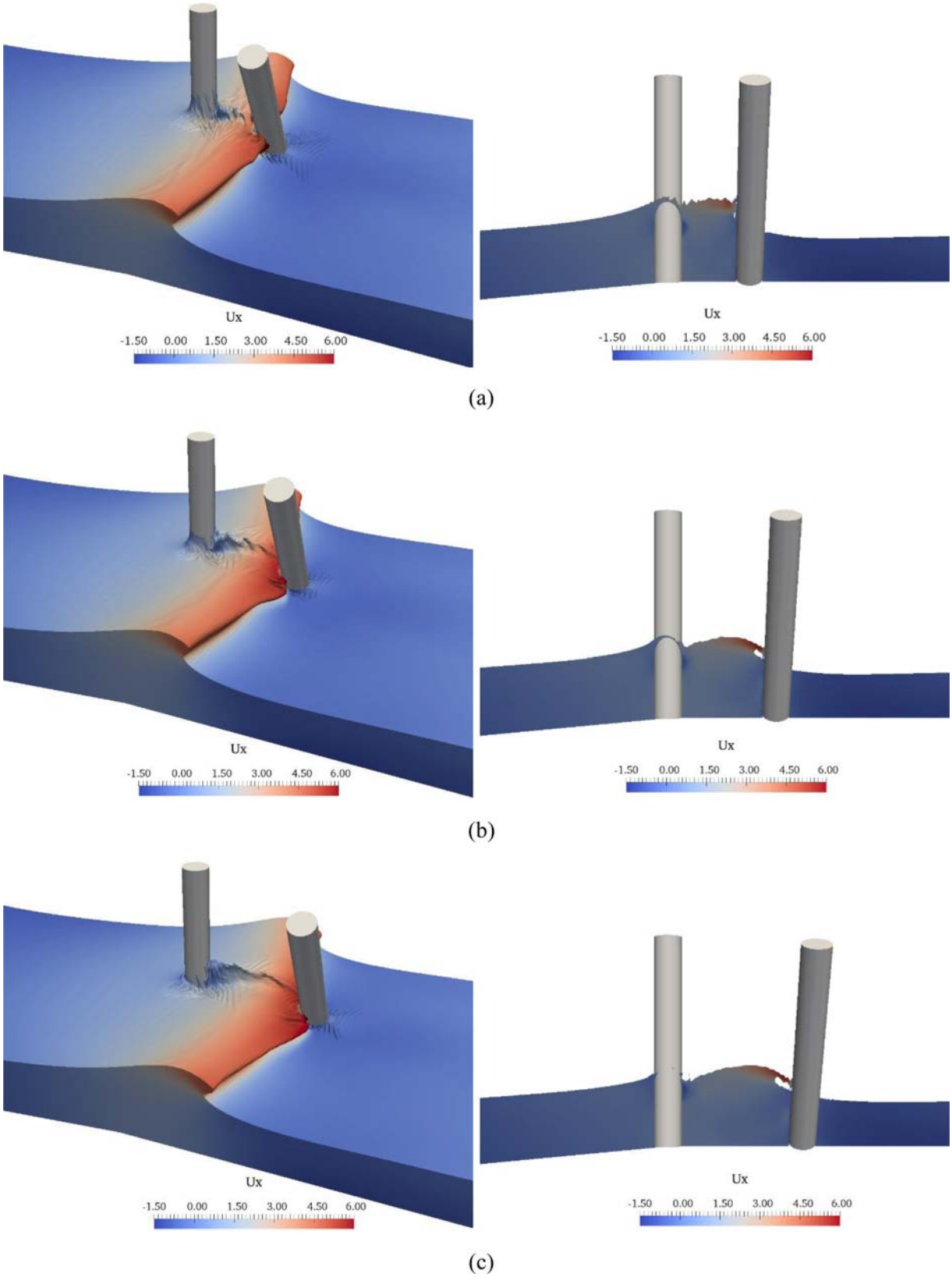

Figure 10. Snapshots of free surface with horizontal velocity contours corresponding to the time of maximum breaking wave force on the downstream cylinder for Scenario C: (a) $S = 3D$; (b) $S = 4D$; (c) $S = 5D$. The left side is a three-dimensional view, and the right side is a section view passing through the central axis of the downstream cylinder and the origin of the coordinates. (This figure is available in colour online.)

between two cylinders is 4D, as shown in Figure 6(b). Moreover, the velocities of water particles on the wave tongue are higher than that in the case of distance $S = 3D$. It causes that the high wave elevation at front surface of the downstream cylinder ($r/D = -0.5$) and the large breaking wave load on the downstream cylinder are obtained when $S = 4D$. For the case of $S = 5D$, the effect of water jet on increasing the wave elevation is weakened. Therefore, the minimum peak value of wave elevation is obtained at the front of the downstream cylinder in Figure 5(b).

Figure 7(a) shows variation characteristics of wave impacting forces F on the downstream cylinder under different separation distance S in one wave period for Scenario B. It clearly shows that the peak of the wave impacting force calculated in the case of $S = 4D$ is higher than that with the cases of other S. The relative variation in peak value of the F is 20.9% when the separation distance varies from $S = 3D$ to $S = 4D$. Figure 7(b) presents the largest free surface elevations before and after the downstream cylinder. Comparison of wave elevations at the same position to the center of the downstream cylinder shows that the peak value of free surface elevation is decreased with S increasing. Furthermore, the gradients of curves from $r/D = -1$ to $r/D = -0.5$ are lower than that under condition Scenario A. It can be explained that the run-up height of the wave in the vertical direction at $r/D = -0.5$ is decreased due to the weaken wave reflection from the downstream cylinder when the inclined angle θ changes from 0° to 15°. Eventually, the lower free surface elevations in front of the downstream cylinder are obtained comparing with Scenario A under the same distance separation S.

Figure 8 presents the free surface with horizontal velocity contours corresponding to the time of maximum breaking wave load on the downstream cylinder for Scenario B. The wave does not overturn when it touches the front surface of the downstream cylinder at the middle section of NWT in Figure 8(a). This is consistent with the calculated result that the wave force curve does not have a sharp peak when $S = 3D$ in Figure 7(a). When the downstream cylinder is placed at a distance of 4D to the upstream cylinder, the phenomenon of overturned wave tongue impacting the downstream cylinder is observed in Figure 8(b). In this circumstance, the downstream cylinder suffering a large breaking wave force reported by Kamath et al. (2016) is also validated in Figure 7(a). With the increasing of S from 4D to 5D, the wave overturns severely and the water particles in front of the wave crest hit the downstream cylinder with small horizontal component velocities, which causes a reduction of horizontal wave force.

Variations of breaking wave impacting forces and peaks of free surface elevations around the downstream cylinder under Scenario C are presented in Figure 9. The maximum breaking wave load is obtained when the distance of two cylinders is 4D, and the minimum value of wave load is occurred for the case of $S = 5D$, as shown in Figure 9(a). It clearly shows in Figure 9(b) that the peaks of the free surface elevations for both in front and behind of the downstream cylinder gradually decrease as S varies from 3D to 5D. The variations of curves from $r/D = -1$ to $r/D = -0.5$ for different S show negative gradients, indicating that the effect of wave run-up height along the cylinder on the free surface elevation at $r/D = -0.5$ is not significant when the downstream cylinder is installed with an inclined angle $\theta = 30°$.

To further study the breaking wave interacting with two tandem cylinders in Scenario C, the free surface with the horizontal velocity contours corresponding to the time of maximum wave load on the downstream cylinder is shown in Figure 10. The wave touches the downstream cylinder with a vertical wavefront when $S = 3D$, as shown in Figure 10(a). The velocity on the wave crest shows low value. In Figure 10(b), the downstream cylinder experiences overturned wave tongue impact with high horizontal velocities. It is the reason that the wave force on the downstream cylinders calculated for the case of $S = 4D$ is higher than that with $S = 3D$. For $S = 5D$ in Figure 10(c), a severely overturned wave impacts on the front surface of the downstream cylinder.

Finally, variations of peak wave impacting forces on the downstream cylinder versus θ under different S are investigated in Figure 11. All the curves of breaking wave forces for different separation distances S decrease first and then increase as θ increases. This can be explained as follows. The front of water jet formed behind the upstream cylinder cannot directly act on the downstream cylinder when θ varying from 0° to 15°. It causes that the local impacting pressure on the downstream cylinder with $\theta = 15°$ has a significant reduction compared with that of $\theta = 0°$. Thus, low wave forces are obtained at $\theta = 15°$. With θ further increasing to30°, the effect of water jet on the local impacting pressure is decreased. However, the submerged area of the downstream cylinder below the still water is increased, which is the reason for the increase in wave force. Furthermore, the peaks of wave forces calculated by $S = 4D$ are larger than that in the cases of $S = 3D$ and $S = 5D$ under the same θ. It is attributed to the fully developed water jet which causes water particles on wavefront impacting the cylinder with high horizontal velocities.

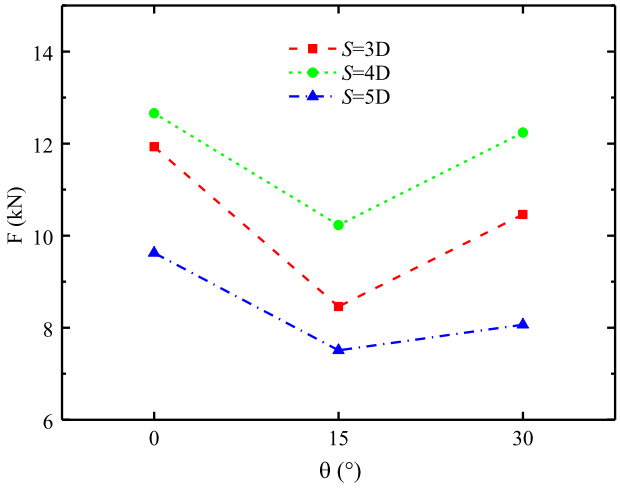

Figure 11. Comparisons of the peak values of breaking wave forces on the downstream cylinder under different Scenarios. (This figure is available in colour online.)

5. Conclusions

The $SST\ k-\omega$turbulence model with the VOF method is employed to simulate the interaction between the breaking waves and two tandem cylinders with different transverse inclined angle and separation distances. Comparisons of the present numerical simulation results and published data indicate that the present numerical model gives good prediction of the breaking wave forces and the free surface elevations. The main conclusions in the present study can be drawn as follows.

(1) The transverse inclined angle of the downstream cylinder has significant effects on the breaking wave loads. With a certain distance between two cylinders, the breaking wave loads on the downstream cylinder decrease first and then increase with the increasing transverse inclined angle θ. The minimum values are obtained with a transverse inclined angle of 15°. The

maximum relative variation of the breaking wave force is reduced 29.1% when the transverse inclined angle changes from 0° to 15° with a separation distance of $S = 3D$.

(2) The peaks of the breaking wave loads on the downstream cylinder increase first and decrease with separation distance varying from 3D to 5D. The largest wave force on the downstream cylinder is 12.66 kN when the downstream cylinder is installed vertically with a separation distance of 4D. It is attributed to the fully developed water jet formed behind the upstream cylinder with a high horizontal velocity hitting the downstream cylinder.

(3) The free surface elevations around the downstream cylinder are related to the separation distance S and transverse inclined angle θ. The maximum free surface elevation in front of the downstream cylinder ($r/D = -0.5$) is observed for the case of $\theta = 0°$ with $S = 4D$, which is due to the high horizontal velocity of water particle and strong wave reflection from the downstream vertical cylinder.

Acknowledgments

The authors are very grateful to the computational resources granted by the Norwegian Metacenter for Computational Science (NOTUR), under Project No: NN9372K. The research work is funded by the National K&D Program of China (project number: 2018YFC0310500).

Disclosure statement

No potential conflict of interest was reported by the author(s).

Funding

This work was supported by Norwegian Metacenter for Computational Science (NOTUR): [Grant Number NN9372K]; National K&D Program of China: [Grant Number 2018YFC0310500].

ORCID

Shengnan Liu http://orcid.org/0000-0001-9612-884X

References

Apelt C, Piorewicz J. 1986. Interference effects on breaking wave forces on rows of vertical cylinders, First Australasian Port, Harbour & Offshore Engineering Conference 1986, Sydney, 29 September-2 October 1986: Preprints of Papers. Institution of Engineers, Australia, p. 191.

Bihs H, Kamath A, Alagan Chella M, Arntsen ØA. 2016. Breaking-Wave interaction with tandem cylinders under different impact scenarios. J Waterway, Port. Coastal, and Ocean Engineering. 142(5):04016005.

Choi S-J, Lee K-H, Gudmestad OT. 2015. The effect of dynamic amplification due to a structure's vibration on breaking wave impact. Ocean Eng. 96:8–20.

Chow AD, Rogers BD, Lind SJ, Stansby PK. 2019. Numerical wave basin using incompressible smoothed particle hydrodynamics (ISPH) on a single GPU with vertical cylinder test cases. Comput Fluids. 179:543–562.

Christensen ED, Bredmose H, Hansen EA. 2005. Extreme wave forces and wave run-up on offshore wind turbine foundations. Proceedings of Copenhagen Offshore Wind. 1–10.

Esandi JM, Buldakov E, Simons R, Stagonas D. 2020. An experimental study on wave forces on a vertical cylinder due to spilling breaking and near-breaking wave groups. Coastal Eng. 162:103778.

Ha Y-J, Kim K-H, Nam BW, Hong SY. 2020. Experimental investigation for characteristics of wave impact loads on a vertical cylinder in breaking waves. Ocean Eng. 209:107470.

Hirt CW, Nichols BD. 1981. Volume of fluid (VOF) method for the dynamics of free boundaries. J Comput Phys. 39(1):201–225.

Irschik K, Sparboom U, Oumeraci H. 2004. Breaking wave loads on a slender pile in shallow water, Coastal Engineering 2004. World Scientific. 4:568–580.

Jacobsen NG, Fuhrman DR, Fredsøe J. 2012. A wave generation toolbox for the open-source CFD library: OpenFoam®. Int J Numer Methods Fluids. 70 (9):1073–1088.

Kamath A, Alagan Chella M, Bihs H, Arntsen ØA. 2016. Breaking wave interaction with a vertical cylinder and the effect of breaker location. Ocean Eng. 128:105–115.

Liu S, Jose J, Ong MC, Gudmestad OT. 2019a. Characteristics of higher-harmonic breaking wave forces and secondary load cycles on a single vertical circular cylinder at different froude numbers. Marine Structures. 64:54–77.

Liu S, Ong MC, Obhrai C. 2019b. Numerical simulations of breaking waves and steep waves past a vertical cylinder at different keulegan-Carpenter numbers. Journal of Offshore Mechanics & Arctic Engineering. 141 (4):041806.

Ma Y, Tai B, Dong G, Perlin M. 2020. Experimental study of plunging solitary waves impacting a vertical slender cylinder. Ocean Eng. 202:107191.

Menter FR, Kuntz M, Langtry R. 2003. Ten years of industrial experience with the SST turbulence model. Turbulence, Heat and Mass Transfer. 4(1):625–632.

Qu S, Liu SN, Ong MC, Sun SZ, Ren HL. 2020. Numerical simulation of breaking wave loading on standing circular cylinders with different transverse inclined angles. Applied Sciences-Basel. 10(4):1347.

Sawaragi T, Nochino M. 1984. Impact forces of nearly breaking waves on a vertical circular cylinder. Coastal Engineering in Japan. 27(1):249–263.

Sparboom U, Oumeraci H, Schmidt-Koppenhagen R, Grüne J. 2005. Large-scale model study on cylinder groups subject to breaking and nonbreaking waves. Proc. 5th International symposium WAVES 2005 Ocean waves measurement and analysis., Madrid, Spain.

Tang Y, Shi W, Ning D, You J, Michailides C. 2020. Effects of spilling and plunging type breaking waves acting on large monopile offshore wind turbines. Frontiers in Marine Science. 7:427.

Wienke J, Sparboom U, Oumeraci H. 2001. Breaking wave impact on a slender cylinder. Coastal Eng. 2000:1787–1798.

Xiao H, Huang W. 2015. Three-Dimensional numerical modeling of solitary wave breaking and force on a cylinder pile in a Coastal surf zone. Journal of Engineering Mechanics. 141 (8):A4014001.